



## RESEARCH LETTER

10.1002/2017GL074341

## Key Points:

- Tsunamis generated by subaerial landslides are challenging to model owing to evolving solid-fluid momentum exchange between deforming bodies
- Our depth-averaged two-phase D-Claw model seamlessly simulates momentum exchange during landsliding and tsunami generation and propagation
- Inundation limits predicted by D-Claw compare well with those observed in satellite imagery of the Tyndall Glacier landslide tsunami

## Supporting Information:

- Movie S1
- Movie S2

## Correspondence to:

D. L. George,  
dgeorge@usgs.gov

## Citation:

George, D. L., R. M. Iverson, and C. M. Cannon (2017), New methodology for computing tsunami generation by subaerial landslides: Application to the 2015 Tyndall Glacier landslide, Alaska, *Geophys. Res. Lett.*, *44*, 7276–7284, doi:10.1002/2017GL074341.

Received 2 JUN 2017

Accepted 23 JUN 2017

Accepted article online 28 JUN 2017

Published online 22 JUL 2017

Published 2017. American Geophysical Union. This article is a US Government work and is in the public domain in the USA.

## New methodology for computing tsunami generation by subaerial landslides: Application to the 2015 Tyndall Glacier landslide, Alaska

D. L. George<sup>1</sup> , R. M. Iverson<sup>1</sup> , and C. M. Cannon<sup>1,2</sup> 

<sup>1</sup>U.S. Geological Survey, Vancouver, Washington, USA, <sup>2</sup>U.S. Geological Survey, Portland, Oregon, USA

**Abstract** Landslide-generated tsunamis pose significant hazards and involve complex, multiphase physics that are challenging to model. We present a new methodology in which our depth-averaged two-phase model D-Claw is used to seamlessly simulate all stages of landslide dynamics as well as tsunami generation, propagation, and inundation. Because the model describes the evolution of solid and fluid volume fractions, it treats both landslides and tsunamis as special cases of a more general class of phenomena. Therefore, the landslide and tsunami can be efficiently simulated as a single-layer continuum with evolving solid-grain concentrations, and with wave generation via direct longitudinal momentum transfer—a dominant physical mechanism that has not been previously addressed in this manner. To test our methodology, we used D-Claw to model a large subaerial landslide and resulting tsunami that occurred on 17 October 2015, in Taan Fjord near the terminus of Tyndall Glacier, Alaska. Modeled shoreline inundation patterns compare well with those observed in satellite imagery.

### 1. Introduction

Coseismic tsunamis such as the 2004 Indian Ocean and 2011 Tohoku tsunamis have widespread impacts, but subaerial landslides that enter water bodies can produce equally destructive waves, albeit at more localized scales. Examples include the 1958 Lituya Bay, Alaska, rockslide ( $\approx 30 \times 10^6 \text{ m}^3$ ) and tsunami, which resulted in the highest known inundation in historical times ( $\approx 525 \text{ m}$ ) [Miller, 1960; Fritz *et al.*, 2001], and more recently, the 2015 Tyndall Glacier, Alaska, landslide ( $70\text{--}80 \times 10^6 \text{ m}^3$ ) [Stark, 2015] and resulting Taan Fjord tsunami. While these tsunamis occurred in largely uninhabited regions, the threat of landslide-generated tsunamis impacting more populous regions is widely recognized [e.g., Synolakis *et al.*, 2002; Okal and Synolakis, 2004; Grilli *et al.*, 2009; Waythomas *et al.*, 2009; Tehranirad *et al.*, 2015]. Efficient, accurate, robust models are needed to understand the physics of landslide-generated tsunamis and to assess the associated hazards.

Landslide-generated tsunamis present unique modeling challenges because of the need to compute landslide dynamics as well as wave-generation and wave-propagation dynamics. Researchers have used a variety of approaches, as summarized in an extensive literature review by Yavari-Ramshe and Ataie-Ashtiani [2016]. Much of this literature is focused on modeling the wave characteristics (nonlinearities, dispersion, etc.) resulting from prescribed and simplified landslide behavior (e.g., motion of a submerged rigid body). Less focus has been directed toward accurately modeling the physics of landslide initiation and motion and the evolving landslide-water interaction. Most modeling efforts that do seek to resolve these earlier stages of the landslide wave-generation process can be broadly categorized as follows: (1) approaches that utilize an independent landslide model that is used to generate boundary conditions for a wave-propagation model [e.g., Adabie *et al.*, 2012; Xing *et al.*, 2016; Grilli *et al.*, 2009], (2) variable-density 3-D multifluid models [e.g., Abadie *et al.*, 2010; Horrillo *et al.*, 2013], and (3) depth-averaged multilayered models in which the landslide material is assumed to completely underlie the water body [e.g., Fernández-Nieto *et al.*, 2010; Ma *et al.*, 2015; Kirby *et al.*, 2016].

The approaches enumerated above all have shortcomings for modeling tsunami generation by subaerial landslides. Use of landslide model output to prescribe boundary conditions for a tsunami model fails to account for bidirectional momentum exchange and conservation. Computationally intensive 3-D models can be illuminating mechanistically but are prohibitively inefficient for application to real-world hazard assessment [Yavari-Ramshe and Ataie-Ashtiani, 2016]. Moreover, 3-D models based on multifluid rheologies fail to account for landslides' complex mechanisms of energy dissipation, which are influenced by dynamical

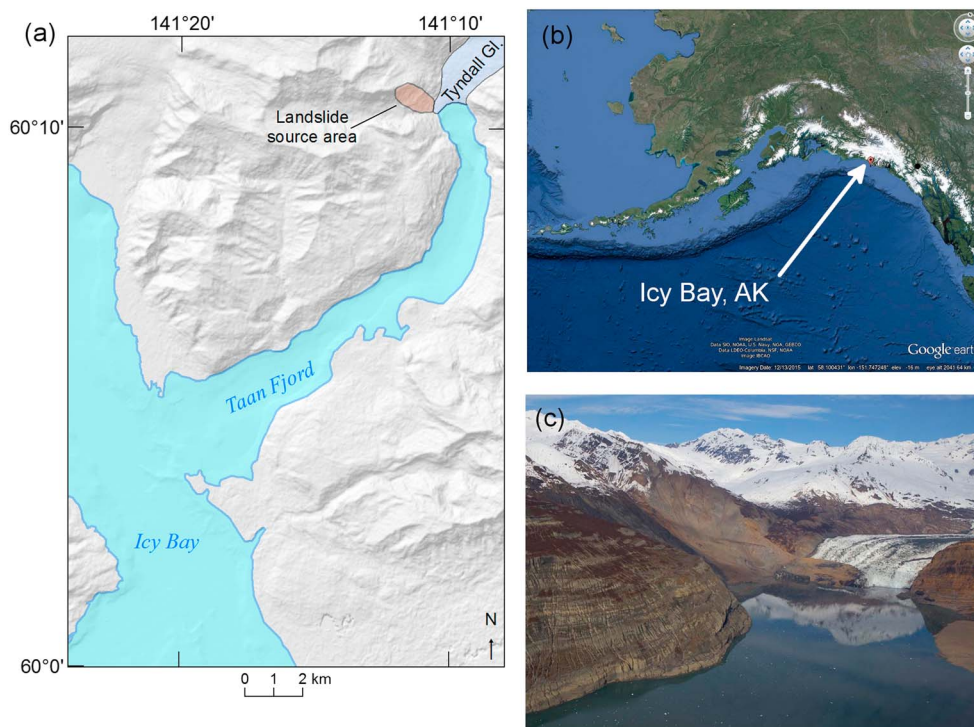


**Figure 1.** The landslide source area (a) in relation to Icy Bay and (b) in relation to southeast Alaska. (c) A photograph taken following the landslide (courtesy of Christopher Larsen, University of Alaska, Fairbanks) provides an oblique view of the Tyndall Glacier terminus and adjacent landslide source area.

feedbacks that cause an evolution of effective friction [Iverson, 2005; Iverson and George, 2016]. Finally, while multilayered depth-averaged models have been successfully applied to tsunamis generated by submarine landslides, they are unsuitable for modeling tsunamis generated by subaerial landslides, wherein the dominant wave-generating mechanisms are due to longitudinal mass displacement and momentum exchange, not to vertical motion of the seafloor. [see Yavari-Ramshe and Ataie-Ashtiani, 2016 for an overview, and results from Fritz *et al.*, 2003a, 2003b; Okal and Synolakis, 2004; Heller and Hager, 2014; Heller, 2007; Xiao and Lin, 2016, and others].

Here we propose use of a new, single-layer, multiphase, depth-averaged model to seamlessly simulate all stages of subaerial landsliding and consequent tsunami generation and propagation. In this model momentum conservation and exchange occurs naturally as the landslide material interacts with the water body and generates impulse waves. This approach is very accurate and efficient computationally, and we apply it without tuning of any calibration parameters. We test our approach by comparing model predictions with tsunami inundation limits observed in satellite imagery, and we also compare our predictions with results obtained using a more traditional methodology.

## 2. The 2015 Tyndall Glacier Landslide and Taan Fjord Tsunami

At about 8:19 P.M. (local time) on 17 October 2015, after a period of heavy rain, a large landslide occurred near the toe of Tyndall Glacier in southeast Alaska [Rozell, 2016; Stark, 2015]. Tyndall Glacier originates on the southwestern flank of Mount St. Elias (elevation 5489 m). U.S. Geological Survey (USGS) aerial photographs show that as recently as 1957, Tyndall Glacier occupied the entire length of Taan Fjord, an arm of Icy Bay (Figure 1). Since 1957, the glacier terminus has receded by about 18 km. Measurements from Landsat imagery show the terminus retreated about 10 km between 1972 and 2000 but retreated minimally between 2000 and 2015. Sometime between 1983 and 1996 a large landslide described by Meigs and Sauber [2000] and by Meigs *et al.* [2006] occurred along the fjord wall near the toe of Tyndall Glacier, but this landslide consisted of a slump that did not run out a great distance or impact the nearby fjord. The landslide of 17 October 2015 remobilized the older slump debris into a high-speed landslide and possibly involved additional material as well. Meigs and Sauber [2000] suggest that the older slump was a result of instability caused by deglaciation

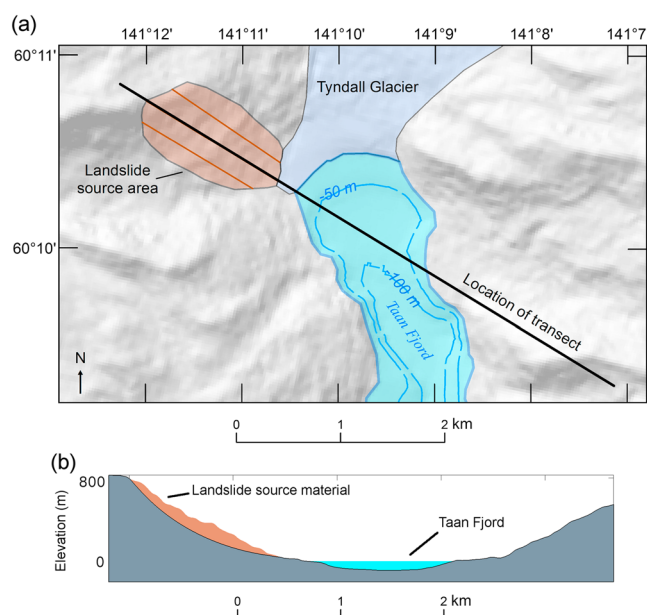


**Figure 2.** (a) Map view and (b) vertical cross-section profile of the landslide source area near the terminus of the Tyndall Glacier. Three longitudinal transects crossing the landslide source identify the location of fitted logarithmic spirals used to estimate the shape of the continuous failure surface. The vertical cross section (Figure 2b) is along the dark transect shown in Figure 2a.

and the consequent increase in valley wall height. However, valley wall height did not significantly increase between 1996 and 2015, so that mobilization of the 2015 landslide cannot be attributed directly to glacier recession.

Runout of the 2015 landslide generated a tsunami in Taan Fjord that reached vertically 150 m up a hillside on the opposite side of the fjord [Rozell, 2016]. Landslide mass estimates from the long-period seismicity radiated by the landslide were about  $1.8 \times 10^{11}$  kg, which implies a volume of about  $70\text{--}80 \times 10^6$  m<sup>3</sup> [Stark, 2015]. To draw further inferences about the scope of the event, we used satellite imagery acquired beforehand and shortly afterward (ASTER, Landsat, and Earth Observing 1-Advanced Land Imager).

### 3. Methods

#### 3.1. Estimating the Landslide Source Geometry and Digital Terrain Model

We outlined the 2015 landslide source area extent by interpreting satellite topography and imagery, guided by mapping of Meigs *et al.* [2006] of the older slump deposit at the site. We approximated the landslide basal slip surface by fitting logarithmic spirals along three longitudinal transects drawn orthogonal to scarps within the landslide (Figure 2). (In lieu of additional data, landslide slip-surface profiles are commonly assumed to have log-spiral shapes.) The logarithmic spirals were constrained by the inferred scarp and toe inclinations, and by the landslide volume estimate of  $70\text{--}80 \times 10^6$  m<sup>3</sup>. The slip surface profiles were joined with the source area outline to form a continuous 3-D surface by using triangulated irregular network interpolation. The consequent modeled landslide source area is 0.9 km<sup>2</sup> and volume is  $78 \times 10^6$  m<sup>3</sup>.

To form a base DEM for our computations, we used a combined bathymetric-topographic terrain model with airborne Interferometric Synthetic Aperture Radar (IFSAR) topography and bathymetry interpolated from U.S. National Atmospheric and Oceanic Administration (NOAA) hydrographic surveys (H09649, H10985, H11100, and H11994), nautical chart 16741 [NOAA, 2012], and depth contours illustrated by Meigs *et al.* [2006]. Bathymetry coverage is incomplete, and manually interpolated contours were used for a  $\approx 6$  km reach between NOAA chart 16741 and the study area of Meigs *et al.* [2006].

#### 3.2. The D-Claw Model

Our depth-averaged landslide and debris flow model, D-Claw, describes the coupled evolution of solid and fluid volume fractions in conjunction with mass and momentum conservation. A key feature of the model is the evolving feedback between the solid-volume fraction and the pore-fluid pressure—an important

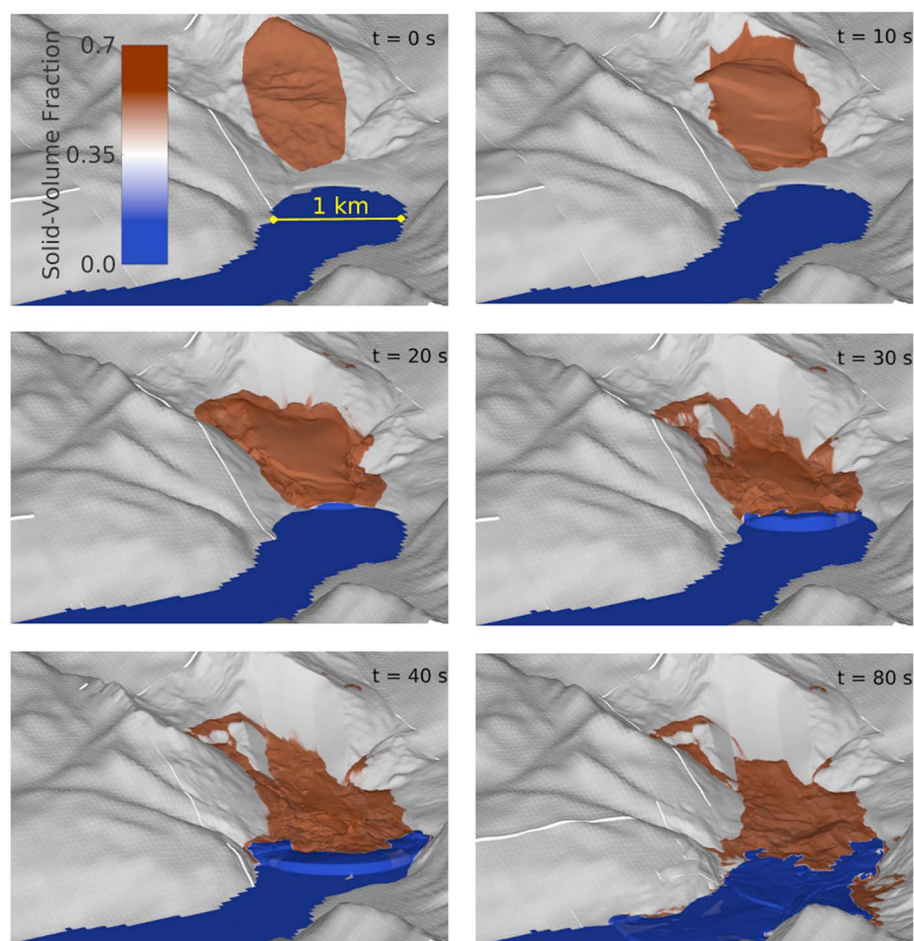


**Figure 3.** The simulated landslide initiation and generation of impulse waves. The color scale indicates the evolving solid-volume fraction. Evolving higher-resolution AMR grids resolve the landslide motion and subsequent wave generation. An animated version of this figure more clearly illustrates the wave generation process and is available in the supporting information.

mechanism known to influence the evolving apparent friction and mobility of landslides [Iverson, 2005; Iverson and George, 2016]. Incorporation of this feedback enables simulation of landslide dynamics from initiation to deposition without imposing unrealistic initial force balances or adjusting rheologies along the runout path [Iverson and George, 2016]. A detailed derivation of the D-Claw equations is provided by Iverson and George [2014], and a detailed description of our numerical solution technique as well as tests of model predictions against experimental data is provided by George and Iverson [2014].

In the limit of vanishing solids fraction, D-Claw's model equations reduce to the nonlinear shallow-water equations that are commonly used for tsunami modeling. In fact, D-Claw provides a generalization and extension of the tsunami modeling software GeoClaw [George, 2006; Berger et al., 2011; LeVeque et al., 2011; Mandli et al., 2016], and it reproduces GeoClaw solutions if solids are absent. Like GeoClaw, D-Claw employs adaptive mesh refinement (AMR), finite-volume shock-capturing algorithms [LeVeque, 2002], inundation-front resolution, and well-balanced preservation of static and flowing steady states [George, 2008, 2011; George and Iverson, 2014].

To model tsunamis generated by subaerial landslides, we initialize D-Claw by representing the landslide source material as a statically balanced, homogeneous grain-water mixture, and by representing the water body as a static pure fluid. Landslide motion is instigated by specifying a gradual rise in basal pore water pressure until failure commences at the weakest point. Ensuing landslide motion satisfies depth-averaged mass and momentum conservation, and impulse waves are generated naturally as the denser landslide mixture impacts the water body and exchanges mass and momentum with it. A key advantage of this approach is that

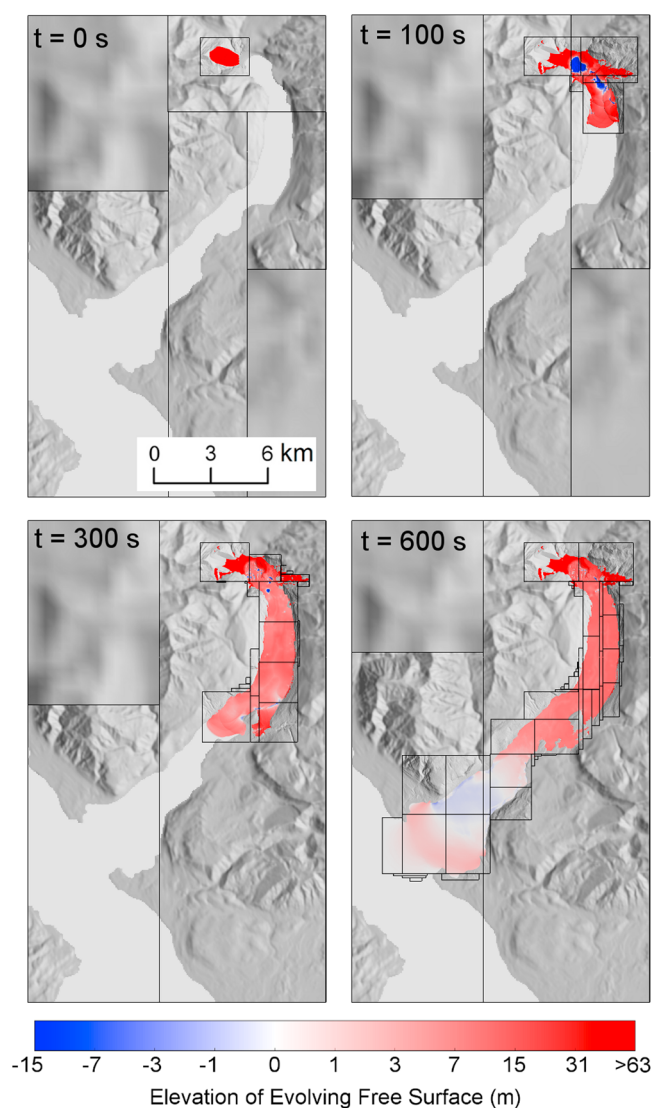


**Figure 4.** Map views of the simulated landslide and tsunami propagation. The blue-red shading indicates the elevation of the evolving free surface relative to the undisturbed water elevation (with 0 m corresponding to  $-1.07$  m mean sea level (msl)). The color scale is based on a  $\log_2$  scale to visually accommodate the highly variable surface height. Rectangular outlines indicate evolving AMR grids. An animated version of this figure provides greater detail and is available in the supporting information.

it does not require specification of coupling mechanisms to link distinct models for landslide motion, wave generation, and wave propagation. If the depth and length scales of the landslide and impacted water body are similar (Figure 2), then the shallowness assumption used to derive the D-Claw equations can be applied to the entire continuum as a single layer—as is commonly done for modeling landslides and tsunamis individually. If the impacted water body is deep relative to the landslide mass, then the single-layer assumption becomes more tenuous and multiple layers that exchange mass and momentum might be warranted.

To generate the chief results we present here, D-Claw was initialized as described above, with pure fluid in Taan Fjord and Icy Bay with a sea surface elevation of  $-1.07$  m (based on NOAA tide gauge records corresponding to the time of the landslide). Model parameters are described in detail by Iverson and George [2014] and George and Iverson [2014]. Because of the current lack of data for physical properties of the Tyndall Glacier landslide material, we used the same parameter values we previously used when modeling the 2014, Oso, Washington landslide, [Iverson and George, 2016]. (An additional parameter necessary for the water body, the Manning friction coefficient, was set to  $0.025 \text{ m}^{-1/3} \text{ s}$ , as done by Berger *et al.* [2011]. We used three levels of adaptive grids, with 400 m, 50 m, and 5 m resolutions. The finest third-level grids are used to resolve all motion of landslide

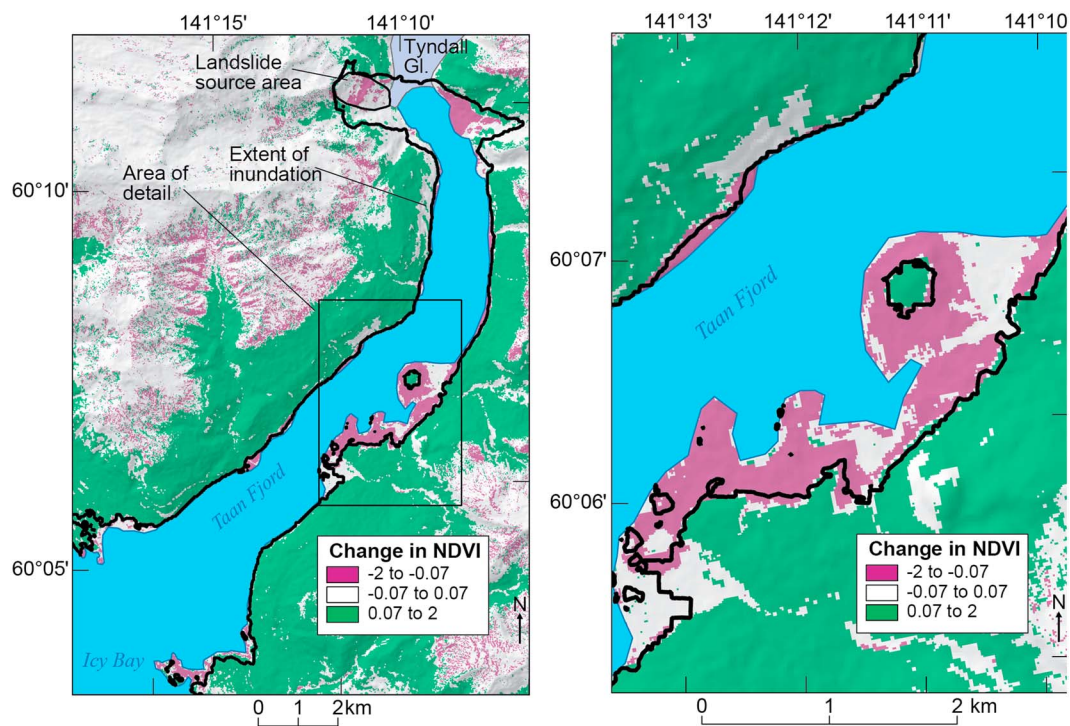


**Figure 5.** NDVI images indicating the decreased vegetation caused by tsunami inundation near the shoreline of the Taan Fjord. The extent of the inundation predicted by D-Claw is outlined in black.

material and water waves. The coarser levels resolve dry land and stationary water prior to the arrival of waves (see Figure 4). The use of AMR in this manner improves computational efficiency by an order of magnitude compared to the use of a single uniform 5 m grid (319 versus 7820 min wall time for 600 s simulation on a MacBook quad-core laptop) [cf. LeVeque et al., 2011].

To help evaluate the results obtained using our new methodology, we also performed more traditional simulations in which we first precomputed the landslide dynamics in the absence of water and then used the computed landslide surface as an evolving basal boundary surface for simulating tsunami generation and propagation. The same model parameters were used for all simulations.

#### 4. Results

We first present results obtained by using our new methodology. Figure 3 provides an oblique perspective of the simulated landslide impacting Taan Fjord. Because of the relative volumes of landslide material and fjord water (Figure 2b), the landslide causes significant mass displacement and longitudinal momentum transfer, generating a large water wave in a piston-like fashion. Figure 4 shows the simulated tsunami wave propagating down Taan Fjord and into Icy Bay.

We utilized satellite imagery to compare observed tsunami inundation limits with those predicted with our new methodology. Aerial imagery taken after the tsunami shows clear signs of inundation and vegetation removal along the shores of Taan Fjord [Rozell, 2016]. We used pan-sharpened Landsat 8 Operational Land Imager images from 14 May 2015 and 15 May 2016 to assess vegetation change. For each image, normalized difference vegetation index (NDVI) was calculated from the visible red (R) and near-infrared (NIR) bands:  $NDVI = (NIR - R)/(NIR + R)$ . High values of NDVI generally correspond to dense vegetation. NDVI results from 2015 were subtracted from results for 2016 to produce a change image shown in Figure 5 (following similar approaches described previously in the literature [e.g., Mancino et al., 2014]). Overall, there is more vigorous vegetation growth in the Taan Fjord area in 2016, but there are conspicuous areas of vegetation removal adjacent to the shoreline. The extent of inundation predicted by the seamless D-Claw simulation is outlined in black in Figure 5. The modeled inundation limits generally correspond well with those observed in the imagery.

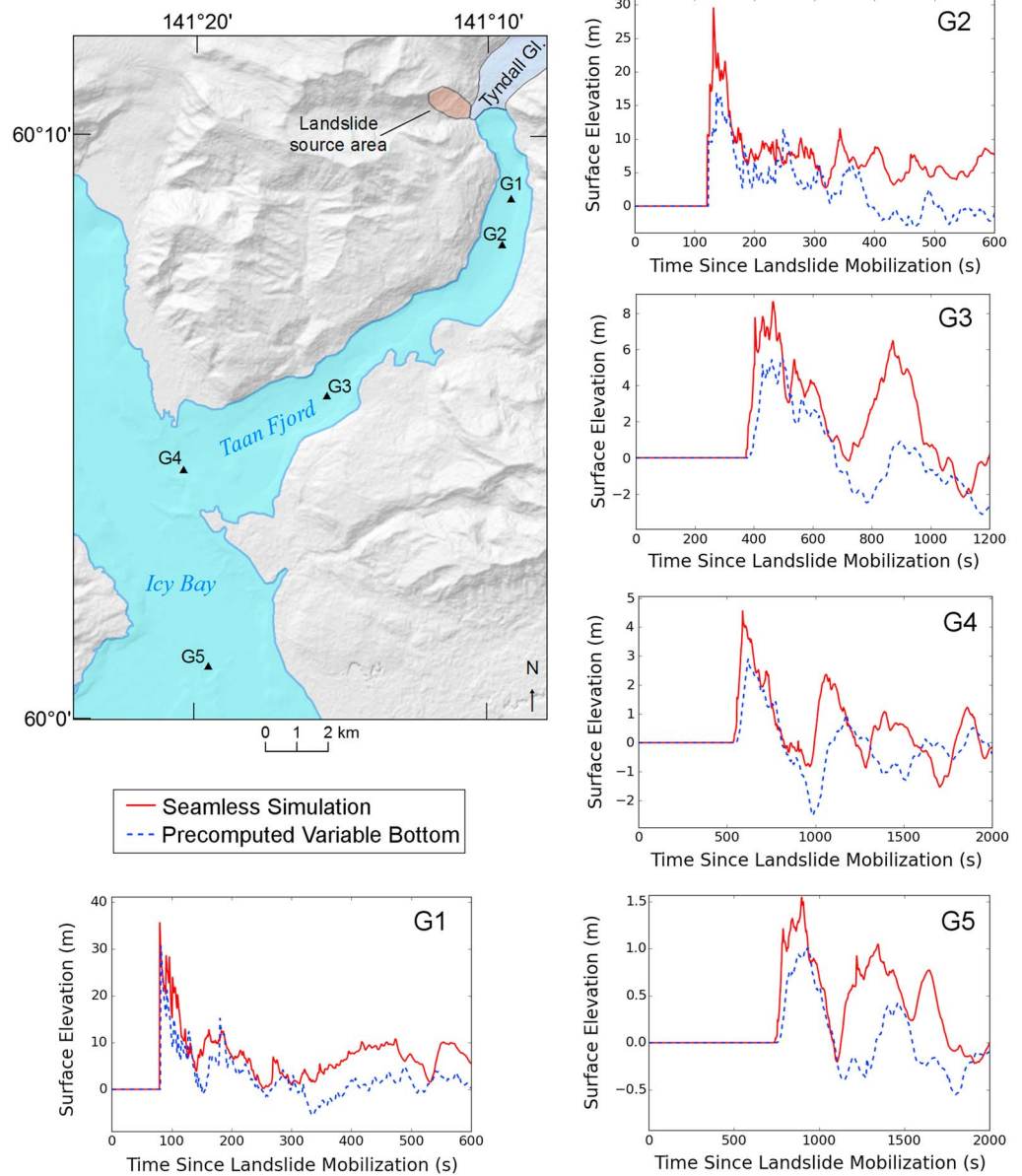


**Figure 6.** Time series of the simulated tsunami at five chosen locations in Taan Fjord and Icy Bay, showing the wave heights relative to the undisturbed water elevation (−1.07 msl). Results of the seamless D-Claw simulation (red) are compared to those of the precomputed variable bottom simulation (dotted blue). Locations of the time series are indicated on the map as triangles near labels G1–G5. All locations are downstream of the reach of significant solid material.

Figure 6 compares results generated by using our new methodology and the more conventional and more labor-intensive boundary-displacement methodology to compute time series of water waves at five locations in Taan Fjord and Icy Bay. Given the dramatically different assumptions about wave generation processes in these alternative approaches, broadly similar tsunami waves are predicted at points distant from the landslide. The seamless D-Claw simulation produces a larger peak amplitude, however—particularly near the source area—and it involves no user intervention to create evolving boundary conditions.

### 5. Discussion

The numerical simulation of tsunamis generated by subaerial landslides poses unique and often competing challenges. The impact of a landslide into a water body is multifaceted and three dimensional, yet a need exists for computationally efficient models for real-world hazard assessment. (The need for efficiency is accentuated

by the increasing call for probabilistic approaches [e.g., Grilli *et al.*, 2009; Yavari-Ramshe and Ataie-Ashtiani, 2016].) Researchers have developed efficient depth-averaged models (particularly multilayered models) for submarine-landslide tsunamis. However, the extension of these models to subaerial landslides and impulse wave generation is numerically challenging (see, e.g., Mandli [2011] for an overview) and physically tenuous. The methodology we present here is exceedingly efficient in terms of machine execution as well as the simulation procedure, and wave generation due to mass displacement and longitudinal momentum exchange occurs naturally. Additionally, use of AMR in D-Claw allows an optimal spatiotemporal resolution of both the landslide and rapidly evolving wave fronts that produce inundation limits. To model the Tyndall Glacier landslide and Taan Fjord tsunami, we employed D-Claw with relatively coarse topographic and bathymetric data that were available prior to the event, and without any model tuning or calibration. Thus, our modeling procedure was closely analogous to procedures that must be used for practical hazard forecasts when no constraints from postevent studies are available.

Because of the relatively short wavelength of landslide-generated tsunamis, there is increasing consensus that wave dispersion, which is neglected in oceanic-scale tsunami models based on the shallow water equations, plays an important role in wave propagation [e.g., Grilli and Watts, 1999; Lynett and Liu, 2002, 2005; Fritz *et al.*, 2004; Zhou and Teng, 2010; Ma *et al.*, 2013; Kim, 2014]. Interestingly, nonhydrostatic pressure corrections for depth-averaged landslide models (that account for the effects of steep and curving basal topography) yield equations similar to those of dispersive Boussinesq-type water-wave models [see Castro-Orgaz *et al.*, 2014]. Incorporation of such correction terms in D-Claw may provide a fruitful direction for future research.

## 6. Conclusions

Our seamless D-Claw simulations of the Tyndall Glacier landslide and Taan Fjord tsunami used an uncalibrated model but produced shoreline inundation patterns that are consistent with the data currently available. More in-depth comparisons would require higher-resolution bathymetry and topography as well as additional field data. Comparisons of two alternative approaches (seamless versus precomputed landslide and evolving seafloor) predict similar tsunami waves in Taan Fjord and Icy Bay. Thus, the two approaches would likely lead to similar assessments of inundation hazards in this particular case. However, the seamless approach using D-Claw has clear computational and methodological advantages because it avoids the step of precomputing an evolving spatiotemporal landslide surface, and the mass and momentum of the system are automatically resolved owing to the absence of quasi-coupled model interfaces. Our results suggest that D-Claw can simulate the impulse waves associated with subaerial landslide tsunamis with sufficient fidelity for hazard forecasting.

### Acknowledgments

The authors wish to thank the Clawpack Team ([www.clawpack.org](http://www.clawpack.org)), Joseph Walder (USGS), Matt Logan (USGS), Andrew Meigs (Oregon State University), Christopher Larsen (University of Alaska, Fairbanks), and Joel Curtis (NWS NOAA, Juneau, AK). The data described herein (basal slip surface, combined topographic-bathymetric DEMs, and NDVI results) are available at [www.sciencebase.gov](http://www.sciencebase.gov) (doi:10.5066/F73R0RR3).

### References

- Abadie, S., D. Morichon, S. T. Grilli, and S. Glockner (2010), Numerical simulation of waves generated by landslides using a multiple-fluid Navier-Stokes model, *Coastal Eng.*, *57*, 779–794.
- Adabie, S., J. C. Harris, S. T. Grilli, and R. Fabre (2012), Numerical modeling of tsunami waves generated by the flank collapse of the Cumbre Vieja Volcano (La Palma, Canary Islands): Tsunami source and near field effects, *J. Geophys. Res.*, *117*, C05030, doi:10.1029/2011JC007646.
- Berger, M. J., D. L. George, R. J. LeVeque, and K. T. Mandli (2011), The GeoClaw software for depth-averaged flows with adaptive refinement, *Adv. Water Resour.*, *34*, 1195–1206, doi:10.1016/j.advwatres.2011.02.016.
- Castro-Orgaz, O., K. Hutter, J. V. Giraldez, and W. H. Hager (2014), Nonhydrostatic granular flow over 3-D terrain: New Boussinesq-type gravity waves?, *J. Geophys. Res. Earth Surf.*, *120*, 1–28, doi:10.1002/2014JF003279.
- Fernández-Nieto, E. D., F. Bouchut, D. Bresch, M. J. Castro-Díaz, and A. Mangeney (2010), A new Savage-Hutter model for submarine avalanches and generated tsunami, *J. Comput. Phys.*, *227*, 7720–7754.
- Fritz, H. M., W. H. Hager, and H.-E. Minor (2001), Lituya Bay case: Rockslide impact and wave run-up, *Sci. Tsunami Hazards*, *19*, 3–22.
- Fritz, H. M., W. H. Hager, and H.-E. Minor (2003a), Landslide generated impulse waves: 1. Instantaneous flow fields, *Exp. Fluids*, *35*, 505–519.
- Fritz, H. M., W. H. Hager, and H.-E. Minor (2003b), Landslide generated impulse waves: 2. Hydrodynamic impact crater, *Exp. Fluids*, *35*, 520–532.
- Fritz, H. M., W. H. Hager, and H.-E. Minor (2004), Near field characteristics of landslide generated impulse waves, *J. Waterw. Port Coastal Ocean Eng.*, *ASCE*, *130*, 287–302.
- George, D. L. (2006), Finite volume methods and adaptive refinement for tsunami propagation and inundation, PhD thesis, Univ. of Washington, Seattle.
- George, D. L. (2008), Augmented Riemann solvers for the shallow water equations over variable topography with steady states and inundation, *J. Comput. Phys.*, *227*(6), 3089–3113, doi:10.1016/j.jcp.2007.10.027.
- George, D. L. (2011), Adaptive finite volume methods with well-balanced Riemann solvers for modeling floods in rugged terrain: Application to the Malpasset dam-break flood (France, 1959), *Int. J. Numer. Methods Fluids*, *66*(8), 1000–1018, doi:10.1002/flid.2298.
- George, D. L., and R. M. Iverson (2014), A depth-averaged debris-flow model that includes the effects of evolving dilatancy: II. Numerical predictions and experimental tests, *Proc. R. Soc. A*, *470*(2170), 20130820.
- Grilli, S. T., and P. Watts (1999), Modeling of waves generated by a moving submerged body. Applications to underwater landslides, *Eng. Anal. Boundary Elem.*, *23*, 645–656.

- Grilli, S. T., O. D. S. Taylor, D. P. Baxter, and S. Marezki (2009), Probabilistic approach for determining submarine landslide tsunami hazard along the upper East Coast of the United States, *Mar. Geol.*, *264*(1–2), 74–97.
- Heller, V. (2007), Landslide generated impulse waves: Prediction of near field characteristics, PhD thesis, ETH Zurich, Zurich.
- Heller, V., and W. H. Hager (2014), A universal parameter to predict subaerial landslide tsunamis?, *J. Mar. Sci. Eng.*, *2*, 400–412.
- Horrillo, J., A. Wood, G.-B. Kim, and A. Parambath (2013), A simplified 3-D Navier-Stokes numerical model for landslide-tsunami: Application to the Gulf of Mexico, *J. Geophys. Res. Oceans*, *118*, 6934–6950, doi:10.1002/2012JC008689.
- Iverson, R. M. (2005), Regulation of landslide motion by dilatancy and pore pressure feedback, *J. Geophys. Res.*, *110*, F02015, doi:10.1029/2004JF000268.
- Iverson, R. M., and D. L. George (2014), A depth-averaged debris-flow model that includes the effects of evolving dilatancy: I. Physical basis, *Proc. R. Soc. A*, *470*(2170), 20130819.
- Iverson, R. M., and D. L. George (2016), Modelling landslide liquefaction, mobility bifurcation and the dynamics of the 2014 Oso disaster, *Géotechnique*, *66*(3), 175–187, doi:10.1680/geot.15.LM.004.
- Kim, J. (2014), Finite volume methods for tsunamis generated by submarine landslides, PhD thesis, Univ. of Washington, Seattle, Wash.
- Kirby, J. T., F. Shi, D. Nicolsky, and S. Misra (2016), The 27 April 1975 Kitimat, British Columbia, submarine landslide tsunami: A comparison of modeling approaches, *Landslides*, *13*, 1421–1434, doi:10.1007/s10346-016-0682-x.
- LeVeque, R. J. (2002), *Finite Volume Methods For Hyperbolic Problems*, *Texts in Appl. Math.*, Cambridge Univ. Press, Cambridge, U. K.
- LeVeque, R. J., D. L. George, and M. J. Berger (2011), Tsunami modeling with adaptively refined finite volume methods, *Acta Numerica*, *20*, 211–289, doi:10.1017/S0962492911000043.
- Lynett, P., and P. L.-F. Liu (2002), A numerical study of submarine-landslide-generated waves and run-up, *Proc. R. Soc. A*, *458*(2028), 2885–2910.
- Lynett, P., and P. L.-F. Liu (2005), A numerical study of the run-up generated by three-dimensional landslides, *J. Geophys. Res.*, *110*, C03006, doi:10.1029/2004JC002443.
- Ma, G., J. T. Kirby, and F. Shi (2013), Numerical simulation of tsunami waves generated by deformable submarine landslides, *Ocean Modell.*, *69*, 146–165.
- Ma, G., J. T. Kirby, T. Hsu, and F. Shi (2015), A two-layer granular landslide model for tsunami wave generation: Theory and computation, *Ocean Modell.*, *93*, 40–55.
- Mancino, G., A. Nolè, F. Ripullone, and A. Ferrara (2014), Landsat TM imagery and NDVI differencing to detect vegetation change: Assessing natural forest expansion in Basilicata, southern Italy, *For. Biogeosci. For.*, *7*(2), 75.
- Mandli, K. T. (2011), Finite volume methods for the multilayer shallow water equations with applications to storm surge, PhD thesis, Seattle, Wash.
- Mandli, K. T., A. J. Ahmadi, M. J. Berger, D. Calhoun, D. L. George, Y. Hadjimichael, D. I. Ketcheson, G. I. Lemoine, and R. J. LeVeque (2016), Clawpack: building an open source ecosystem for solving hyperbolic PDEs, *PeerJ Comp. Sci.*, *2*, e68.
- Meigs, A., and J. Sauber (2000), Southern Alaska as an example of the long-term consequences of mountain building under the influence of glaciers, *Quat. Sci. Rev.*, *19*, 1543–1562.
- Meigs, A., W. C. Krugh, K. Davis, and G. Bank (2006), Ultra-rapid landscape response and sediment yield following glacier retreat, Icy Bay, southern Alaska, *Geomorphology*, *78*(3–4), 207–221.
- Miller, D. J. (1960), The Alaska earthquake of July 10, 1958: Giant wave in Lituya Bay, *Bull. Seismol. Soc. Am.*, *50*(2), 253–266.
- NOAA (2012), *Icy Bay: Nautical Chart 16741*, edited by 12th ed. scale 1:40,000, U.S. Dep. of Commerce National Oceanic and Atmospheric Administration (NOAA), Washington, D. C.
- Okal, E. A., and C. E. Synolakis (2004), Source discriminants of near-field tsunamis, *Geophys. J. Int.*, *158*, 899–912.
- Rozell, N. (2016), *The Giant Wave of Icy Bay*, Geophys. Inst. AK Press Release, Fairbanks, Alaska. [Available at <http://www.gi.alaska.edu/alaska-science-forum/giant-wave-icy-bay>.]
- Stark, C. P. (2015), Landslide dynamics from seismology: New results, Abstract EP51D-08 presented at 2015 Fall Meeting, AGU, San Francisco, Calif., 14–18 Dec.
- Synolakis, C. E., J.-P. Bardet, J. C. Borrero, H. L. Davies, E. A. Okal, E. A. Silver, S. Sweet, and D. R. Tappin (2002), The slump origin of the 1998 Papua New Guinea tsunami, *Proc. R. Soc. A*, *458*, 763–790.
- Tehrani, B., J. C. Harris, A. R. Grilli, S. T. Grilli, S. Abadie, J. T. Kirby, and F. Shi (2015), Far-field tsunami impact in the North Atlantic basin from large scale flank collapses of the Cumbre Vieja Volcano, La Palma, *Pure Appl. Geophys.*, *172*, 3589–3616.
- Waythomas, C. F., P. Watts, F. Shi, and J. T. Kirby (2009), Pacific Basin tsunami hazards associated with mass flows in the Aleutian arc of Alaska, *Quat. Sci. Rev.*, *28*, 1006–1019.
- Xiao, H., and P. Lin (2016), Numerical modeling and experimentation of the dam-overtopping process of landslides-generated waves in an idealized mountainous reservoir, *J. Hydraul. Eng.*, *142*(12), 1–12, doi:10.1061/(ASCE)HY.1943-7900.0001203.
- Xing, A., Q. Xu, Y. Zhu, J. Zhu, and Y. Jiang (2016), The August 27, 2014, rock avalanche and related impulse water waves in Fuquan, Guizhou, China, *Landslides*, *13*, 411–422.
- Yavari-Ramshe, S., and B. Ataie-Ashtiani (2016), Numerical modeling of subaerial and submarine landslide-generated tsunami waves—Recent advances and future challenges, *Landslides*, *13*(6), 1325–1368, doi:10.1007/s10346-016-0794-2.
- Zhou, H., and M. H. Teng (2010), Extended fourth-order depth-integrated model for water waves and currents generated by submarine landslides, *J. Eng. Mech.*, *136*(4), 506–516.